



Induced effect of tungsten incorporation on the catalytic properties of CeVO₄ systems for the selective reduction of NO_x by ammonia



Sylvain Gillot^a, Grégory Tricot^b, Hervé Vezin^b, Jean-Philippe Dacquin^a, Christophe Dujardin^a, Pascal Granger^{a,*}

^a Univ. Lille, CNRS, Centrale Lille, ENSCL, Univ. Artois, UMR 8181 – UCCS – Unité de Catalyse et Chimie du Solide, F-59000 Lille, France

^b Laboratoire de Spectrochimie Infrarouge et Raman, UMR CNRS 8516, Bâtiment C5, 59650 Villeneuve d'Ascq, France

ARTICLE INFO

Keywords:

Ammonia
CeV_{1-x}W_xO₄ mixed oxides
Fast-SCR
Selective catalytic reduction
NO_x

ABSTRACT

The SCR performances of aged W-doped CeVO₄ catalysts were investigated in fast-, NO₂- and standard conditions. Bulk CeV_{1-x}W_xO₄ catalysts were prepared in soft conditions, according to a hydrothermal synthesis route at 180 °C leading to the *ad hoc* tetragonal structure. The aging procedure consisted in exposing the samples to 10 vol.% H₂O diluted in air at 600 °C. The impact of this aging process was investigated as a function of tungsten loading, with x varying in the range 0.02–0.15. A clear beneficial effect is distinguishable at high temperature, i.e., above 300 °C, associated to a sharp selectivity enhancement irrespective of the operating conditions and tungsten loading. On the contrary, a slight detrimental effect on the reaction rate is clearly discernible in standard-conditions below 300 °C. It was found that the thermal aging induces more extensive diffusion of V⁵⁺ species assisted by the presence of substituted W⁶⁺. It was also demonstrated that tungsten diffuses more readily than V⁵⁺ leading ultimately to a significant surface enrichment and the formation of Ce₄W₉O₃₃ mixed oxide evidenced from XRD and Raman spectroscopy. Hence, tungsten would rather act as a stabilizer than promoter avoiding the sintering of monomeric VO_x species to more active polyvanadate species but also less selective. The gain observed in selectivity at high temperature can be equally explained by a greater stabilization of Brønsted acid sites and the preservation of the dispersion of monomeric vanadate species preventing the occurrence of ammonia oxidation.

1. Introduction

Supported vanadium catalysts on titania, doped by various metal oxide additives [1,2] are currently used for the ammonia Selective Catalytic Reduction (SCR). Now, V₂O₅-WO₃/TiO₂ is recognized as a benchmark for the abatement of NO_x from stationary emission sources [3,4]. The optimal composition of vanadium and tungsten is generally below 2 wt.% and 10 wt.%, respectively, corresponding to a remarkable selectivity behavior in the presence of a large excess of oxygen [3,5]. In fact, such an optimization in the past three decades was not an easy task and has been the subject of numerous investigations [6–11], which sometimes led to controversial statements regarding the nature of active and selective vanadium species as a function of their coverage. Today, there is a general agreement which emphasizes the fact that isolated VO_x species, stabilized in distorted tetrahedral environment, can polymerize to more active metavanadates species at increasing vanadium loading but becoming at the same time less selective than isolated vanadium species. On the contrary, the role of tungsten still

remains unclear leading to conflicting viewpoints for explaining the specific interactions between tungsten, vanadium and/or TiO₂ which can originate significant improvements in the selectivity and in the acidic properties of the surface through the formation of Brønsted acid sites [3]. Alemany et al. [12] previously suggested that tungsten would act as spectator allowing a closer proximity of isolated vanadium oxo centers to form most active dimeric V–O–V structures. On the contrary, Komppio et al. [13] found that tungsten would mainly originate a dilution effect, privileging an intimate mixing between tungsten and vanadia instead of the formation of oxidic vanadium islands. Hence, according to Alemany et al. [12], tungsten would mainly act as stabilizer rather than promoter in agreement with previous investigations [14]. However, a closer interaction between W and V can also lead to more reducible vanadium species which can attest improved redox properties of vanadium moieties.

More recently, V₂O₅-WO₃/TiO₂ catalysts were developed for automotive applications especially the urea-Selective Catalytic Reduction (urea-SCR). It is obvious that today, there is a strong renewed interest

* Corresponding author.

E-mail address: pascal.granger@univ-lille1.fr (P. Granger).

likely associated to this latter practical application [13,15,16] in order to promote the tolerance of V_2O_5 - WO_3 / TiO_2 catalysts to contaminants in fossil fuels and biodiesel, as well as their hydrothermal resistance. Indeed, well-dispersed vanadia species are usually sensitive to thermal sintering above 650 °C. Their aggregation can ultimately lead to V_2O_5 clusters that can sublime in the temperature conditions and enhance the formation of undesired N_2O . These phenomena considerably limit their automotive applications [17,18].

Recent developments of bulk vanadium-free catalysts led to successful achievements with the discovery of hydrothermally stable CeO_2 - WO_3 / TiO_2 compared to benchmarks up to 670 °C exposed in 5 vol.% water in air for 64 h [19]. Previous attempts also demonstrated that the incorporation of rare earths to V_2O_5 - WO_3 / TiO_2 prevents a loss of specific surface through the transformation of anatase to rutile and favors the formation of more thermally stable rare earth vanadate species [20]. Recently, iron vanadates supported on titania (9 wt.% $FeVO_4$ / TiO_2) revealed improved performances thanks to a high dispersion of $FeVO_4$, a higher density of defective sites and electronic inductive effects between Fe^{3+} and V^{5+} [21]. Interestingly, the authors explained that the peculiar properties of those catalysts were ascribed to VO_x surface enrichment originating high ammonia-SCR activity and durability [21,22]. Such explanations match correctly with our recent observations on bulk $CeVO_4$ -SCR catalysts: Unreducible V^{5+} species stabilized in tetrahedral geometry of the zircon-type structure of $CeVO_4$ can diffuse at the surface and aggregate into more reducible polymeric species [23]. Such reconstructions led to unprecedented performances at 200 °C compared to homologous supported VO_x / CeO_2 catalyst [24] reflected by a sharp increase of the normalized rates, shifting from 11.9 to 171.5 $\mu\text{mol s}^{-1} \text{m}^{-2}$, for the standard-SCR [23]. This rate enhancement was found closely dependent on the aging conditions and could be viewed as the stabilization of more stable segregated 2D- VO_x species than those currently obtained on more classical alumina and silica supports conventionally prepared via a simple wet impregnation method. Such stronger interactions have been already characterized, allowing higher dispersion limit reaching 9–12 V atoms per nm^2 of ceria support [25]. The coexistence of ceria with vanadia sample can also lead to more complex surface properties ascribed to V–O–V and V–O–Ce surface structures that can also originates diverse acidic and redox sites [26].

The present study deals with the incorporation of tungsten to $CeVO_4$ catalysts for the selective reduction of NO_x by ammonia. Particular attention will be paid to the impact of W in monitoring the nature of dispersion of segregated oxidic vanadium species and their relative stability especially if tungsten can act as spectator playing the role of spacer and/or modifying the relative reactivity of VO_x entities through the formation of mixed metallic oxide compounds that could enhance the Brønsted acidity suggested as a crucial parameter in SCR catalysis.

2. Experimental

2.1. Catalyst preparation

$CeV_{1-x}W_xO_4$ were prepared according to a classical hydrothermal route as described elsewhere [27,28]. First, Na_3VO_4 (99.98% Sigma-Aldrich) was dissolved in 50 ml of dionized water under vigorous stirring. An aqueous solution of nitric acid (3 M) was added dropwise until reaching a pH value of 1.8 corresponding to the stabilization of VO_2^+ cations. Afterwards, an aqueous solution obtained from the dissolution of $Ce(NO_3)_3 \cdot 6H_2O$ and $(NH_4)_6H_2W_{12}O_{40} \cdot xH_2O$ precursors (supplied by Sigma-Aldrich) was added to the former solution containing VO_2^+ cations. An aqueous solution of sodium hydroxide (1 M) was added dropwise to enable the precipitation of the hydroxide precursors. The suspension thus obtained, with pH stabilized at 8.5, was hydrothermally treated at 180 °C for 24 h, to promote the formation of the zircon-type structure for $CeV_{1-x}W_xO_4$ mixed oxides with x varying in the range 0–0.15. The solid samples were recovered by centrifugation,

abundantly washed with dionized water and finally with ethanol. After drying in air at 80 °C for 24 h, freshly-prepared samples, labeled “fresh” $CeV_{1-x}W_xO_4$, were aged at 600 °C, exposed to a gas mixture composed of 10 vol.% H_2O diluted in air with a space velocity of 0.024 g h^{-1} . The elemental analysis, performed by Energy Dispersive X-ray Spectroscopy, did not reveal detectable loss of vanadium and tungsten induced by the thermal aging under wet atmosphere.

2.2. Physicochemical characterization

2.2.1. Bulk characterization

X-Ray diffraction (XRD) measurements were carried out on a Bruker AXS D8 Advance diffractometer in Bragg-Brentano geometry fitted with a LynxEye Super Speed detector. XRD patterns were recorded with $Cu K\alpha$ radiation ($\lambda = 0.154 \text{ nm}$, 40 kV, 30 mA) in the 10–80° 2θ range with a 0.02° 2θ step.

Raman spectroscopy analysis was performed on a Labram HR Jobin Yvon spectrometer. Spectra were recorded by using an excitation wavelength of 532 nm. The calibration was systematically checked by a silicon line at 520 cm^{-1} .

H_2 -Temperature-Programmed Reduction experiments (H_2 -TPR) were performed on a Micromeritics Autochem II 2920 instrument with a flow of 5 vol.% H_2 diluted in Ar and at constant gradient temperature of 10 °C min^{-1} .

The ^{51}V magic angle spinning nuclear magnetic resonance (MAS-NMR) experiments were performed at 210.4 MHz on a 18.8 T AVANCE III Bruker NMR spectrometer. The spectra were acquired with a 3.2 mm probehead with a spinning frequency of 22 kHz, a 0.5 μs pulse length (corresponding to a $\pi/12$ flip angle), 1024–2048 transients and a recycle delay of 0.5 s. Additional experiments were performed at a spinning frequency of 20 kHz to discriminate between the isotropic signals and the spinning sidebands (denoted with (*) in the following). The ^{51}V chemical shifts were referred to $VOCl_3$ solution as 0 ppm.

Continuous wave electronic paramagnetic resonance (CW-EPR) experiments were acquired on an X-band ELEXYS E580 Bruker spectrometer at room temperature with 256 transients, 2 mW of microwave power and 2 G of modulation amplitude.

2.2.2. Surface characterization

Specific surface area was calculated from N_2 physisorption measurements at –196 °C with a Flowsorb III device. Prior physisorption, samples were cleaned at 100 °C for 1 h under a flow of helium at ambient pressure.

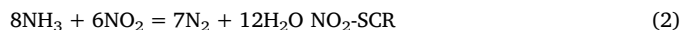
X-ray Photoelectron Spectroscopy (XPS) analysis was performed on an AXIS Ultra DLD Kratos spectrometer fitted with a mono-chromatized aluminium source for excitation (150 W). Binding energies (B.E.) values were calibrated compared to the O 1s B.E. centered at 530.5 eV as internal reference.

Ammonia adsorption-desorption experiments were carried out on a Micromeritics Autochem II 2920 instrument. Ammonia concentration in the outlet mixture was monitored by an Omnistar™ Pfeiffer Mass Spectrometer. Prior to experiments, the samples were outgassed under helium at 500 °C. Temperature-programmed desorption experiments were performed under He on pre-adsorbed samples at 100 °C with a temperature ramp of 10 °C min^{-1} .

Infrared spectra recorded during pyridine adsorption-desorption experiments were recorded on a Nicolet Protégé 460 infrared spectrometer equipped with MCT detector (4 cm^{-1}). The samples were preliminary outgassed under vacuum (10^{-5} mbar) at 450 °C. Pyridine adsorption was performed at room temperature up to saturation coverage. IR spectra were recorded at after desorption under vacuum at different temperatures. The normalized concentration of Lewis and Brønsted acid sites were quantified based on the integrated IR bands taking into account absorption coefficients of respectively $1.5 \text{ cm } \mu\text{mol}^{-1}$ and $1.8 \text{ cm } \mu\text{mol}^{-1}$ [29].

2.3. Catalytic measurements

Temperature-Programmed Reaction (TPR) experiments were performed in a fixed bed flow reactor on 80 mg of catalyst in powder form, with grain size in the range 150–300 µm, diluted in 1 g SiC. The temperature gradually increased at a constant heating rate of 2 °C min⁻¹ from 120 °C to 550 °C. The total flow rate was fixed at 20 L h⁻¹ to obtain a space velocity of 4×10^{-3} g h L⁻¹. The reaction mixture was composed of 400 ppm NH₃, 400 ppm NO_x, 8 vol.% O₂, 10 vol.% CO₂, 10% H₂O diluted in He. Temperature-programmed conversion and selectivity profiles vs. temperature were successively recorded in fast-, NO₂- and standard-SCR conditions (see Eqs. (1)–(3)) corresponding to molar NO to NO_x ratios of respectively 0.5, 0.3 and 1.



N₂ and N₂O concentrations were monitored by online Varian CP-4900 µGC analyses after separation of the reactants and products on two distinct columns (molecular sieve 5 Å and porapak Q). NO_x (NO + NO₂) concentrations were measured by using a Thermo Scientific Model 42i-HL IR spectrometer. The absence of significant external diffusion limitations was previously checked on fresh CeVO₄. Indeed, no significant deviation on the rate of NO conversion was observed by modifying the catalyst loading keeping constant the space velocity [23]. We also verified that we fulfilled the boundary conditions given by Eq. (4) representing the Weisz-Prater criterion [30], taking into account r_{obs} the observed reaction rate expressed in mol m⁻³ s⁻¹, C_{obs} the observed concentration of NO in the gas phase in mol m⁻³, D_{eff,NO} the effective diffusivity for NO expressed in m² s⁻¹ in the range 1.0–1.5 × 10⁻⁶ m s⁻¹ [31] and L = d_p/6 the volume to surface ratio of the grain in m. Hence, internal mass transfer phenomena should not occur significantly, insuring a preferential kinetic regime below 300 °C.

$$\frac{r_{\text{obs}} L^2}{C_{\text{obs}} D_{\text{eff,NO}}} < 1 \quad (4)$$

3. Results

3.1. Bulk physicochemical characterization of CeVO₄

3.1.1. X-ray diffraction analysis

Two series of XRD patterns are collected in Fig. 1 obtained on fresh and aged CeV_{1-x}W_xO₄. As observed in Fig. 1(A), the intense X-ray diffraction peaks at $2\theta = 24.0^\circ$, 32.3 and 47.8° characterize the typical (200), (112) and (312) reflections of the tetragonal structure of CeVO₄ (JCPDS PDF 12-0757) [23,28]. A successive incorporation of tungsten induces a shift on all the reflections to higher 2θ values with a rise in tungsten loading which evidences the formation of a solid solution via the substitution of V⁵⁺ by W⁶⁺ having comparable ionic radii (54 pm vs. 60 pm respectively). Additional reflections also appear assigned to the typical cubic structure of CeO₂ (JCPDS PDF 34-0394) which forms during the hydrothermal synthesis as earlier explained [32]. Let us note that no bulk detectable WO₃ species (JCPDS PDF 32-1395) was observed on fresh samples consistent with a preferential diffusion of W⁶⁺ into the tetragonal structure of CeVO₄. Fig. 1(B) shows that the characteristic reflections of CeVO₄ still predominate on aged samples at 600 °C. However, the shift previously observed on the characteristic 2θ values has disappeared (see Fig. 1(C)). This observation could be closely related to the appearance of additional weak X-ray lines at $2\theta = 25.5^\circ$, 26.0°, 26.6 and 48.5° on CeV_{0.85}W_{0.15}O₄ ascribed to the formation of Ce₄W₉O₃₃ (JCPDS PDF 25-0192) [32,33].

The average crystallite size diameter, calculated according to the Scherrer equation, becomes much lower on tungsten doped samples

compared to the benchmark CeVO₄ which suggests a greater resistance to thermal sintering. A lower crystallite size for CeO₂ is also remarkable on aged tungsten doped samples compared to un-doped parent systems.

3.1.2. Raman spectroscopy

Raman spectra recorded on parent CeO₂ and V₂O₅ and CeV_{1-x}W_xO₄ samples are collected in Fig. 2. CeO₂ is characterized by an unique narrow band at 466 cm⁻¹ ascribed to F_{2g} vibration of its cubic fluorite structure (see Fig. 2(A))–f. Raman lines observed on parent V₂O₅ at 994 cm⁻¹ and below 800 cm⁻¹ correspond to terminal V=O bond and V–O–V structure associated to the symmetric and antisymmetric stretching vibration modes of polyvanadate species [34,35]. Interestingly, they are not observed on CeV_{1-x}W_xO₄ suggesting the absence of bulk segregation of V₂O₅. Raman active modes on fresh CeV_{1-x}W_xO₄ appear at 261, 383, 788, 800 and 863 cm⁻¹ characteristic of a tetragonal structure [36]. The Raman band at 863 cm⁻¹ was earlier ascribed to the breathing mode of VO₄³⁻ in agreement with the tetrahedral environment of vanadium in the zircon-type structure of CeVO₄. The Raman bands at 800 and 788 cm⁻¹ characterize the F_g and B_{2g} antisymmetric stretching modes of vanadate while the active modes at 467 and 383 cm⁻¹ correspond to the B_{2g} and B_{1g} deformations. Interestingly, there is no Raman line at 806, 714 and 271 cm⁻¹ characterizing respectively the W–O stretching mode (A_{1g}, E_g) and W–O–W bending mode (F_{2g}) currently observed for WO₃ which possesses a ReO₃ structure [37]. As observed in Fig. 2(B), two additional weak Raman lines at 925 and 950 cm⁻¹ are distinguishable on aged CeV_{0.85}W_{0.15}O₄ tentatively related to the formation of well-crystallized Ce₂(WO₄)₃ [37].

3.1.3. ⁵¹V NMR and EPR spectroscopy

The ⁵¹V MAS-NMR spectra are reported in Fig. 3. The analyses of fresh CeV_{1-x}W_xO₄ samples (Fig. 3(A)) are composed of a main signal at ~ 437 ppm accompanied by spinning sidebands (denoted with (*)) and a very low intensity (< 1%) signal discernible at ~ 530 ppm. The NMR analyses show that the V/W substitution modifies the NMR signal by slightly shifting the position (toward shielded values) and by increasing the signal broadness compared to the parent CeVO₄. Both modifications are characteristic of slight structural distortions due to partial vanadium substitution by tungsten. It is also noteworthy that the low intensity signal, which has not been assigned, experiences a slight deshielding effect indicating that this signal is also affected by the V/W substitution. Similar observations can be made for the 600 °C aged samples but in much lower extent. As observed, only slight changes are discernible on the main signal broadness and position compared to signals recorded on fresh samples, suggesting the occurrence of bulk reconstruction during ageing at 600 °C ascribed to a partial extraction of tungsten. It also noteworthy that the low intensity signal proportion is even smaller in this sample series. The absence of signal at ~ 609 ppm in all the NMR spectra (fresh and aged samples) also confirm the absence of bulk V₂O₅ segregation.

The room temperature CW-EPR spectra are reported in Fig. 4. The EPR analyses of the untreated samples (Fig. 4(A)) do not exhibit paramagnetic species except for CeV_{0.9}W_{0.1}O₄ sample for which a weak transition is observed at g factor of 1.97 that can be attributed to W⁵⁺ species. In the case of the aged samples at 600 °C (Fig. 4(B)), the EPR analyses do not show any signal for CeVO₄ and CeV_{0.98}W_{0.02}O₄. On the other hand, CeV_{0.95}W_{0.05}O₄ and CeV_{0.85}W_{0.15}O₄ present spectra with typical 8 lines isotropic signals that can be assigned to V⁴⁺ (S = 1/2 I = 7/2) species with a g factor of 1.95 and A_{iso} of 78 G. CeV_{0.9}W_{0.1}O₄ produces a different EPR signal that is characteristic of the W⁵⁺ species as observed in case of the untreated sample.

As recently discussed on aged CeVO₄ [23], the characterization of hyperfine structures on vanadia-based systems have been already described [18,38–40] arising on reduced materials or calcined at high temperature and related to magnetic interaction between unpaired electron with ⁵¹V nucleus of isolated VO²⁺ moieties in square pyramidal or distorted octahedral environment [38,40]. The detection of V

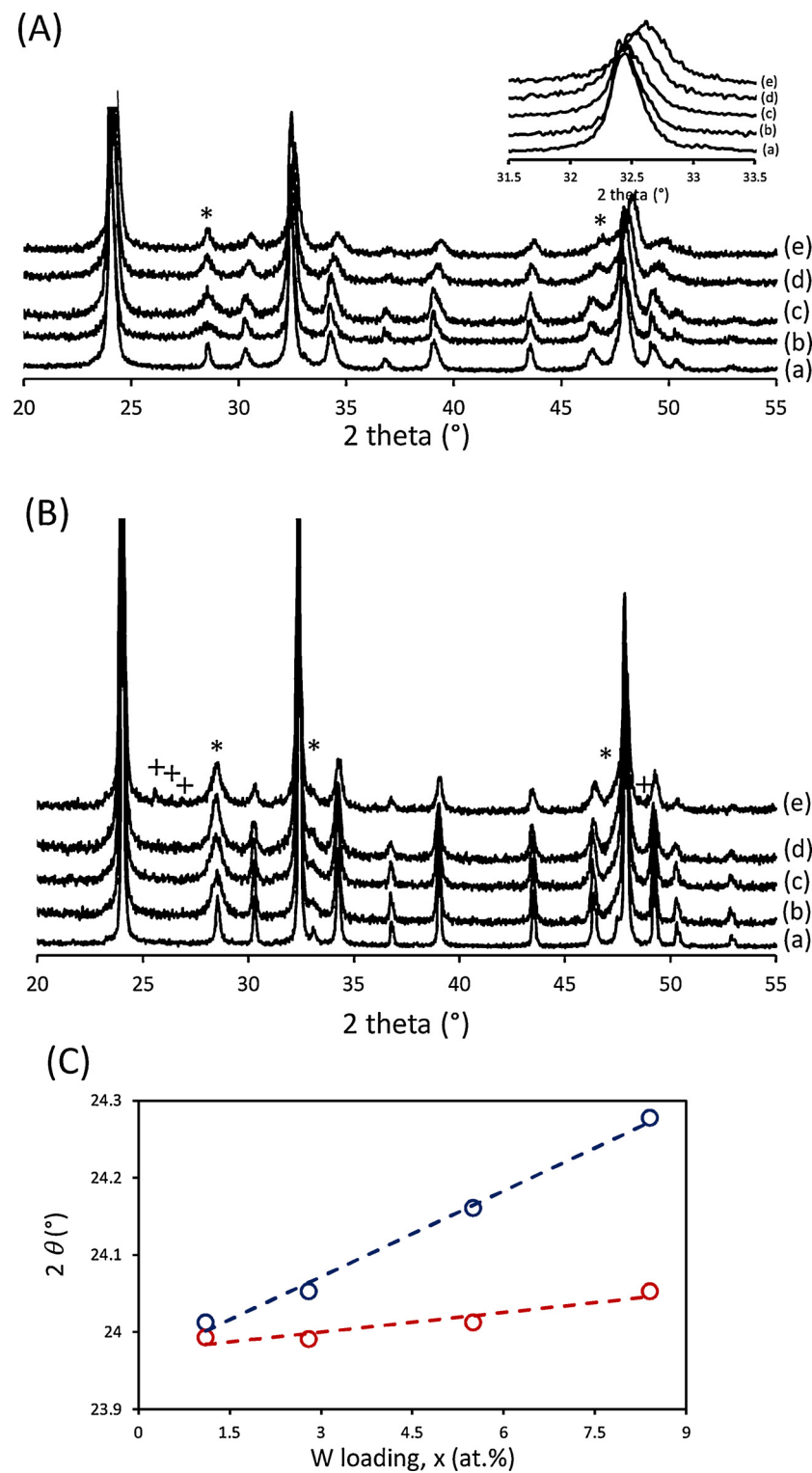


Fig. 1. XRD patterns on fresh CeV_{1-x}W_xO₄ samples (A), after *ex situ* aging in wet atmosphere (air + 10 vol.% H₂O) at 600 °C (B) with x = 0 (a); x = 0.02 (b); x = 0.05 (c); x = 0.10 (d); x = 0.15 (e). Evolution of 2θ position of the (112) reflection assigned to the tetragonal structure of CeV_{1-x}W_xO₄ (C) : fresh sample in blue and aged sample in red – (*) Characteristic reflections of the cubic structure of CeO₂ – (+) Characteristic reflections of Ce₄W₉O₃₃. (For interpretation of the references to colour in this figure legend, the reader is referred to the web version of this article).

(+ IV) species on V₂O_x-WO₃/Al₂O₃ calcined at 900 °C was earlier explained to the agglomeration of isolated vanadyl species into polymeric ones [18]. Clearly, the appearance of this hyperfine structure on highly loaded tungsten samples would emphasize a weaker stability of substituted V⁵⁺ in tetrahedral coordination due to stronger distortions induced by substituted W⁵⁺ species. This could explain the aggregation

of more reducible vanadium species.

3.1.4. Reducibility of CeVO₄ samples

The H₂ consumption profiles vs. temperature obtained on CeV_{1-x}W_xO₄ are compared in Fig. 5. A prominent H₂ consumption takes place above 600 °C, previously ascribed to the bulk reduction of V⁵⁺ to V³⁺

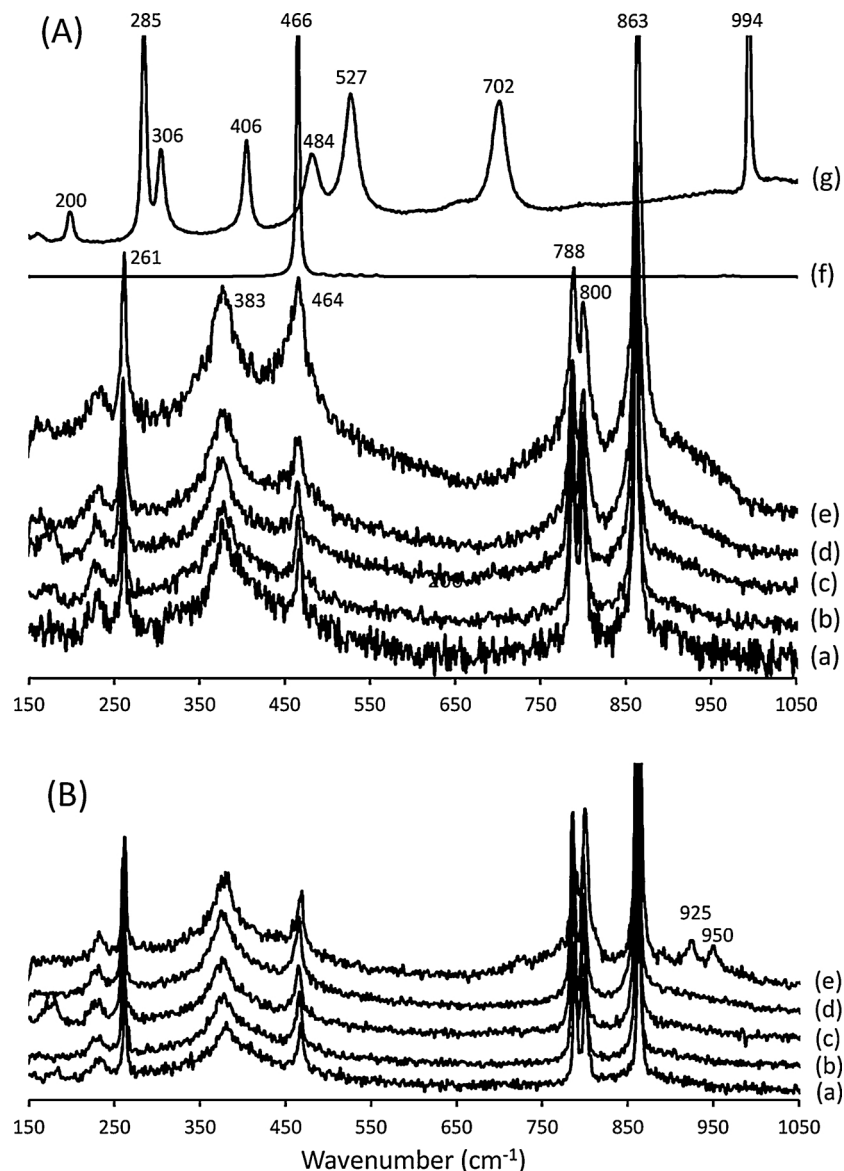


Fig. 2. Raman spectra recorded on fresh CeW_{1-x}V_xO₄ (A) and after aging in *ex situ* conditions in wet atmosphere (air + 10 vol.% H₂O) at 600 °C (B) with x = 0 (a); x = 0.02 (b); x = 0.05 (c); x = 0.10 (d); x = 0.15 (e); CeO₂ (f) and V₂O₅ (g).

leading to the ultimate formation of CeVO₃ [23]. It is worthwhile to note that for x ≤ 0.05 a progressive shift of the maximum temperature to higher values is observable corresponding to a decrease in CeVO₄ crystallite size (see Table 1). A discontinuity is clearly distinguishable for x > 0.05 since the maximum temperature remains unchanged with tungsten loading. Although, this change is still independent on the crystallite size, this discontinuity could reflect a back diffusion of W⁶⁺ species at the surface consistent with the characterization of mixed cerium-tungsten oxides from XRD and Raman spectroscopy analysis.

Weak and broad signals are also discernible below 700 °C appearing at 583 °C on CeVO₄ while two distinct weak surface H₂ reduction processes occur on CeV_{1-x}W_xO₄ at two different ranges of temperature compared to CeVO₄, i.e., 535–549 °C and 613–658 °C. As earlier discussed, the weak H₂ uptake on CeVO₄ at 583 °C would correspond to the reduction of surface Ce⁴⁺ species to Ce³⁺ [41] both in CeO₂ and CeVO₄. However, the reduction of surface VO_x species in this temperature range could not be completely ruled out in agreement with Li et al. [42] who observed the reduction of VO_x species on binary VO_x–CeO₂ systems below 580 °C with a reducibility altered by the strength of interaction on small and large CeO₂ particles.

Now regarding, the weak reduction process in the temperature range 600–660 °C, similar trends as those previously mentioned for the bulk reduction process are observable related to a shift on the maximum temperature and the same discontinuity observed for x > 0.05. Hence, this surface process could reflect the influence of the substitution of V by W for x ≤ 0.05. On the other hand, the discontinuity observed at higher tungsten loading could be related a partial segregation of WO_x species and/or the formation of Ce-W mixed oxides in agreement with XRD and Raman spectroscopy analysis.

3.2. Surface characterization

3.2.1. Nitrogen physisorption

Specific surface areas in Table 1 reveal a detrimental effect of thermal aging which attenuates on tungsten-doped samples. The S_{exp}/S_{theor} ratio represents the surface lost by agglomeration between crystal domains with S_{exp} and S_{theor} corresponding to the experimental specific surface area calculated from the crystallite size of CeV_{1-x}W_xO₄ respectively. As observed, the loss of specific surface area after aging is essentially related to crystallite growth.

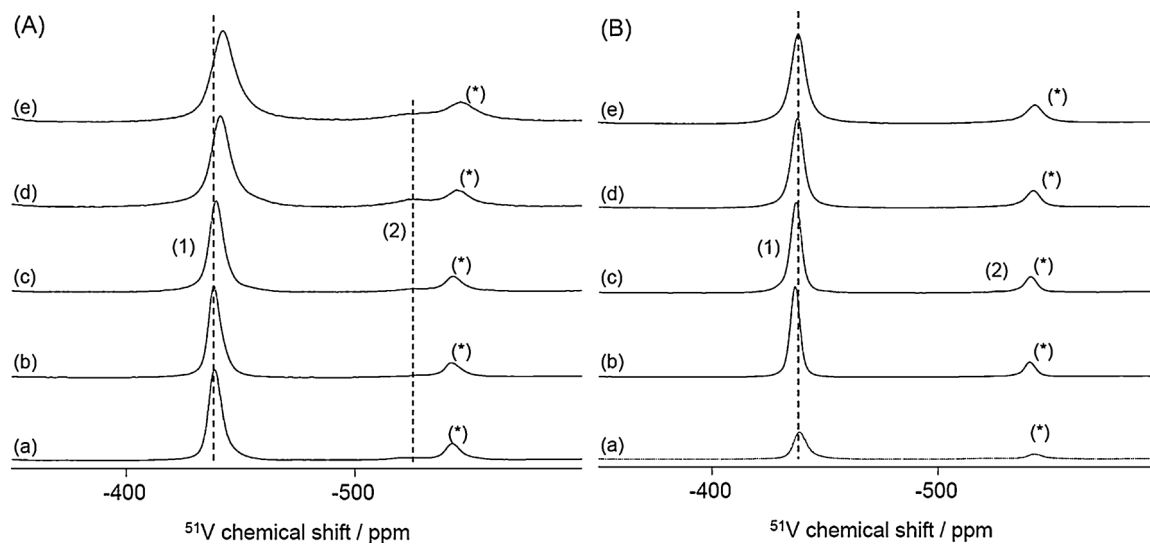


Fig. 3. ^{51}V NMR spectra recorded on fresh (A) and aged $\text{CeV}_{1-x}\text{W}_x\text{O}_4$ at 600°C – $x = 0$ (a); $x = 0.02$ (b); $x = 0.05$ (c); $x = 0.1$ (d); $x = 0.15$ (e).

3.2.2. XPS analysis

The characteristic core level of Ce 3d, W 3d, V 2p and O 1s photopeaks were investigated. XPS data collected in Table 2 do not reveal significant changes on the B.E. values of W 3d_{5/2} and V 2p_{3/2} core levels, near 247.9 eV and 517.7 eV respectively, characteristic of W^{6+} and V^{5+} species [43]. As already demonstrated, Ce 3d core level exhibits more complex features [23,44]. As described in Fig. S1 (see Supplementary materials), the decomposition spectra leads to different contributions with relative intensity depending on $\text{Ce}^{4+}/\text{Ce}^{3+}$ ratio shows a predominant stabilization of Ce^{3+} and a minor contribution of Ce^{4+} stabilized as CeO_2 . Regarding the O 1s photopeak, two contributions arise near 530.5 and 532.0 eV ascribed respectively to lattice oxygen O^{2-} species (O_β) and adsorbed oxygen species (O_α) reflecting the density of defective sites created at the surface of $\text{CeV}_{1-x}\text{W}_x\text{O}_4$ [45,46]. By examining the numerical values in Table 2, no relevant comparison can be drawn. On the other hand, it is noticeable that a thermal aging at 600°C leads to lower $\text{Ce}^{4+}/\text{Ce}^{3+}$ values irrespective of vanadium and tungsten loadings. Such an observation could be explained by the higher sensibility of $\text{CeV}_{1-x}\text{W}_x\text{O}_4$ than CeO_2 to thermal sintering as reported elsewhere [23]. This explanation is consistent with the lower crystallite size for CeO_2 compared to those calculated on aged $\text{CeV}_{1-x}\text{W}_x\text{O}_4$ samples (see Table 1). Based on this, lower Ce/V ratio should be expected. However, the opposite trend is verified up to

$x = 0.05$ similarly to previous observations [23]. Such slight increase in concentration of vanadium suggest a partial diffusion of bulk V^{5+} stabilized in the $\text{CeV}_{1-x}\text{W}_x\text{O}_4$ lattice to the surface. On the other hand, the stabilization of the Ce/V ratio for high tungsten loading would suggest that tungsten plays a key role by blocking this process and/or diluting extracted V^{5+} segregated at the surface. This latter hypothesis seems plausible by examining the W/Ce and V/W ratios which reveal a significant surface W enrichment becoming more accentuated after ageing.

3.3. Catalytic performances of aged $\text{CeV}_{1-x}\text{W}_x\text{O}_4$ in ammonia-SCR

The catalytic properties of aged $\text{CeV}_{1-x}\text{W}_x\text{O}_4$ were measured from successive temperature-programmed experiments at different NO/NO_x ratios, i.e., 1, 0.5 and 0.3, corresponding respectively to standard-, fast- and NO₂-SCR conditions. NO_x conversion and N₂O selectivity profiles vs. temperature are reported in Fig. 6. Optimal rate of NO_x conversion corresponds to the fast SCR-conditions according to Eq. (1) with conversion higher than 90% below 250°C on tungsten doped samples. A loss of conversion usually takes place above 450°C corresponding to a greater production of N₂O. The high level of conversion of NO_x to nitrogen at low T has been earlier ascribed to a faster re-oxidation of vanadate species by NO₂ and/or ad-NO_x species compared to gaseous oxygen [47,48]. Let us note that tungsten substitution significantly

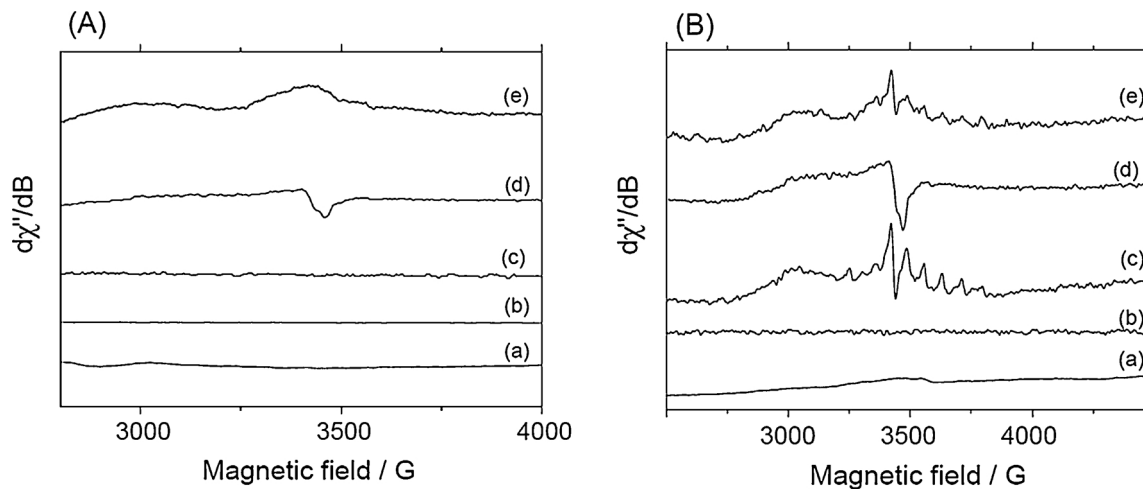


Fig. 4. EPR spectra recorded on fresh (A) and aged $\text{CeV}_{1-x}\text{W}_x\text{O}_4$ at 600°C – $x = 0$ (a); $x = 0.02$ (b); $x = 0.05$ (c); $x = 0.1$ (d); $x = 0.15$ (e).

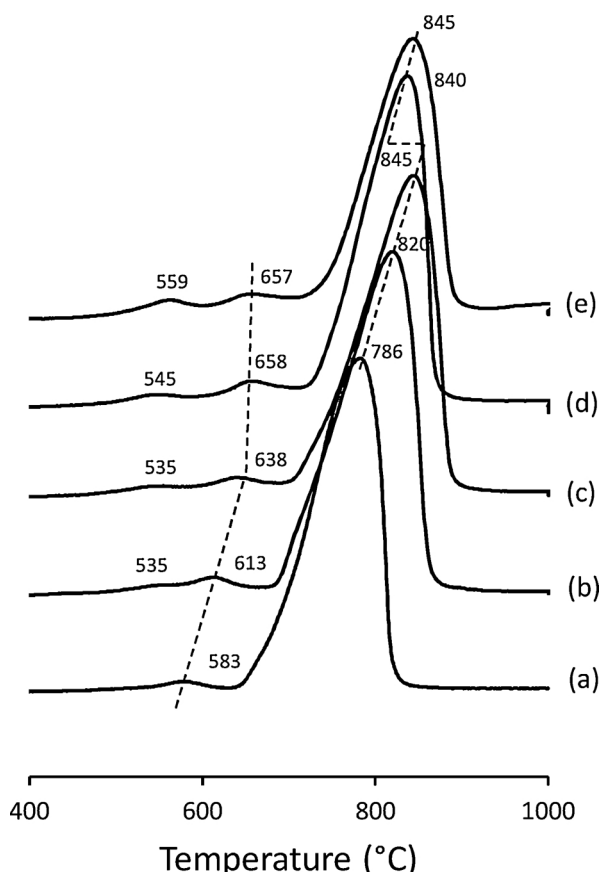


Fig. 5. H_2 -Temperature-programmed consumption profiles recorded on aged $\text{CeV}_{1-x}\text{W}_x\text{O}_4$ at 600°C : $x = 0$ (a); $x = 0.02$ (b); $x = 0.05$ (c); $x = 0.10$ (d); $x = 0.15$ (e).

Table 1
Elemental analysis, textural and structural properties of $\text{CeV}_{1-x}\text{W}_x\text{O}_4$ catalysts freshly-prepared from hydrothermal synthesis and after aging.

Catalyst	Elemental composition (at.%)			Specif. Surf. Area ($\text{m}^2 \text{g}^{-1}$)	$S_{\text{exp}}/S_{\text{theor}}^{\text{a}}$	Crystallite size d (nm)	
	Ce	V	W			$\text{CeV}_{1-x}\text{W}_x\text{O}_4$	CeO_2
CeVO_4 fresh	50.7	49.3	–	46.6	0.97	27	46
CeVO_4 (600°C)	50.1	49.9	–	5.8	0.39	85	57
$\text{CeV}_{0.98}\text{W}_{0.02}\text{O}_4$ fresh	52.9	46.0	1.1	41.0	0.82	25	n.m.
$\text{CeV}_{0.98}\text{W}_{0.02}\text{O}_4$ (600°C) ^b	52.2	46.7	1.1	13.9	0.87	79	13
$\text{CeV}_{0.95}\text{W}_{0.05}\text{O}_4$ fresh	52.0	45.3	2.7	56.2	0.93	21	n.m.
$\text{CeV}_{0.95}\text{W}_{0.05}\text{O}_4$ (600°C) ^b	51.9	45.3	2.8	18.3	0.78	37	10
$\text{CeV}_{0.9}\text{W}_{0.1}\text{O}_4$ fresh	51.8	42.7	5.5	57.0	0.91	20	n.m.
$\text{CeV}_{0.9}\text{W}_{0.1}\text{O}_4$ (600°C) ^b	51.8	42.7	5.5	18.7	0.53	36	20
$\text{CeV}_{0.85}\text{W}_{0.15}\text{O}_4$ fresh	51.7	39.9	8.4	56.8	0.88	20	n.m.
$\text{CeV}_{0.85}\text{W}_{0.15}\text{O}_4$ (600°C) ^b	51.5	41.1	8.5	18.3	0.48	33	19

^a $S_{\text{theor}} = 6.10^3 / (\rho \cdot d)$.

^b After aging at 600°C in wet conditions (air + 10 vol.% H_2O).

improves the rate of NO_x conversion and broadens the operating window at high temperature leading to lower N_2O production but still detected at 550°C . Interestingly, an optimal kinetic regime is reached for $x \geq 0.05$ corresponding to higher conversion levels. For standard-

SCR conditions, i.e., in the absence of NO_2 , a volcano-type curve is observed emphasizing the role played by NO_2 as key intermediate. Its formation at low temperature, via NO oxidation, is usually kinetically limited in standard conditions inducing low NO_x conversion to N_2 . At high temperature some kinetic and thermodynamic limitations must be also taken into account associated to NO oxidation to NO_2 thermodynamically unfavored and/or the occurrence of parallel undesired reactions, i.e., ammonia oxidation. It is worthwhile to note that the conversion curves in standard- and fast-conditions are quasi superimposed above 500°C which suggest the same kinetic behaviour. However, the remarkable selectivity behaviour in standard conditions related to the absence of N_2O production differs from that observed in fast-SCR conditions. This would suggest that the loss of NO_x conversion observed at high temperature likely involves different reaction pathways in standard and fast-conditions. Interestingly, we still observed higher conversion levels for $x \geq 0.05$.

In NO_2 -SCR conditions, one can observe a mixed regime with intermediate NO_x conversions between those recorded in fast- and standard conditions. On the other hand, the same behaviour as that reported in fast conditions seems to occur at high temperature still associated to a greater extent of N_2O production.

Kinetic data have been roughly estimated from temperature-programmed conversions recorded in standard-SCR conditions taking a plug flow reactor mass balance equation into account and conversion values below 300°C . The reaction rate can be approximated according to Eq. (5) assuming reaction orders for NO and NH_3 concentration equal to 1 and ~ 0 respectively below 300°C [49–53]. These hypotheses agree with an Eley-Rideal mechanism currently accepted on vanadia based catalysts and taking into account strong adsorption of ammonia and weak interaction of NO on vanadia surface [50]. Then Eq. (6) can be derived according to first-order kinetics where k stands for the reaction rate constant, F_0 the total molar flow rate, W the mass of catalyst and X_{NO_x} the conversion of NO .

$$r = A \exp\left(-\frac{E_a}{RT}\right) [\text{NO}] \quad (5)$$

$$k = \frac{F_0}{W} \ln\left(\frac{1}{1 - X_{\text{NO}_x}}\right) \quad (\text{mol g}^{-1} \text{s}^{-1}) \quad (6)$$

$$\text{with } k = A \exp\left(-\frac{E_{\text{app}}}{RT}\right). \quad (7)$$

The pre-exponential (A) and the apparent activation energy (E_{app}) (see Eq. (7)), calculated from the values of the intercept and the slopes of the Arrhenius plots in Fig. 7, are collected in Table 3. As previously discussed, the numerical values are slightly lower than those earlier reported over supported vanadium-based catalysts varying normally in the range 35 – 55 kJ mol^{-1} [23,49–53]. Nevertheless, it was shown that this low values would not evidence perturbations due to diffusional limitations especially on CeVO_4 aged at 600°C exhibiting the lowest values. In this latter case it has been hypothesized that changes in the nature of the slow step with the occurrence of surface diffusion processes on the aged sample at 600°C would be more responsible of such low activation barrier [23]. A significant increase in E_{app} on substituted tungsten samples is noticeable for $x \geq 0.02$ compared to the parent CeVO_4 samples shifting from ~ 10 to $\sim 21 \text{ kJ mol}^{-1}$ then stabilizing for higher tungsten compositions. Interestingly, a compensation effect is observed with the same evolution observed on pre-exponential factor. Such evolutions observed on E_{app} and A seem in relative good agreement with those observed on the normalized rate constants expressed per m^2 in Table 3.

Further comparisons with benchmark supported $\text{V}_2\text{O}_5\text{-WO}_3\text{/TiO}_2$ is useful in Table 4 emphasizing remarkable performances of parent and tungsten-doped CeVO_4 catalysts. By comparing the operating conditions, one has to mention that our kinetic measurements were performed in the presence of high concentration of water compared to

Table 2XPS analysis of fresh and aged CeV_{1-x}W_xO₄ catalysts.

Catalyst	B.E. (eV) ^a			Surf. Composition ^a				
	Ce 3d _{5/2}	V 2p _{3/2}	W 3d _{5/2}	V/Ce	W/Ce	V/W	Ce ⁴⁺ /Ce ³⁺	O _α /O _β
CeVO ₄ fresh	883.7	517.6	–	0.78 (0.97)	–	–	0.12	0.34
CeVO ₄ (600 °C) ^b	883.5	517.7	–	0.94 (1.00)	–	–	0.23	0.27
CeV _{0.98} W _{0.02} O ₄ fresh	883.4	517.7	247.9	0.96 (0.87)	0.13 (0.02)	7.4 (43.5)	0.20	0.37
CeV _{0.98} W _{0.02} O ₄ (600 °C) ^b	883.3	517.7	247.8	1.05 (0.89)	0.16 (0.02)	6.6 (43.5)	0.32	0.35
CeV _{0.95} W _{0.05} O ₄ fresh	883.4	517.6	248.0	0.89 (0.87)	0.13 (0.05)	6.8 (17.4)	0.22	0.35
CeV _{0.95} W _{0.05} O ₄ (600 °C) ^b	883.4	517.7	248.0	0.96 (0.87)	0.32 (0.05)	3.0 (17.4)	0.31	0.58
CeV _{0.9} W _{0.1} O ₄ fresh	883.4	517.7	248.0	0.80 (0.82)	0.21 (0.11)	3.8 (7.5)	0.23	0.65
CeV _{0.9} W _{0.1} O ₄ (600 °C) ^b	883.4	517.7	248.0	0.79 (0.82)	0.40 (0.11)	2.0 (7.5)	0.34	0.46
CeV _{0.85} W _{0.15} O ₄ fresh	883.3	517.7	247.9	0.86 (0.77)	0.27 (0.16)	3.2 (4.8)	0.22	0.46
CeV _{0.85} W _{0.15} O ₄ (600 °C) ^b	883.4	517.7	248.0	0.82 (0.80)	0.41 (0.17)	2.0 (4.8)	0.30	0.43

^a Binding energy values and surface composition from XPS analysis.^b After aging in wet conditions (air + 10 vol.% H₂O) bulk compositions from elemental analysis are in brackets.

dried operating conditions selected elsewhere [18,53]. Water usually induces a significant detrimental effect on the SCR reaction and must be considered for practical applications. Despite those more severe operating conditions, we did not observe the formation of N₂O especially at high temperature when ammonia oxidation occurs significantly in standard-conditions. This kinetic feature would reflect a higher thermal stability as already pointed out on aged CeVO₄ [23]. Indeed, subsequent aggregation of isolated to polymeric vanadates species currently lead to intrinsically more active sites but recognized as less selective [18]. It seems obvious that tungsten could play a crucial role slowing down this process.

4. Discussion

The influence of partial substitution of vanadium by tungsten in bulk CeVO₄ catalytic systems on the selective catalytic reduction of NO_x by ammonia has been investigated in this study with the aim to understand the peculiar role played by tungsten still under debate on supported vanadia-based systems [12–14]. Hence, one of the main issues of this paper was to get more insights into the induced effects of tungsten on the structural properties of surface vanadium species, acting as stabilizer or promoter, and their related impacts on the catalytic properties in terms of activity and selectivity with the occurrence of competitive oxidation and reduction reactions, i.e., NO_x reduction to

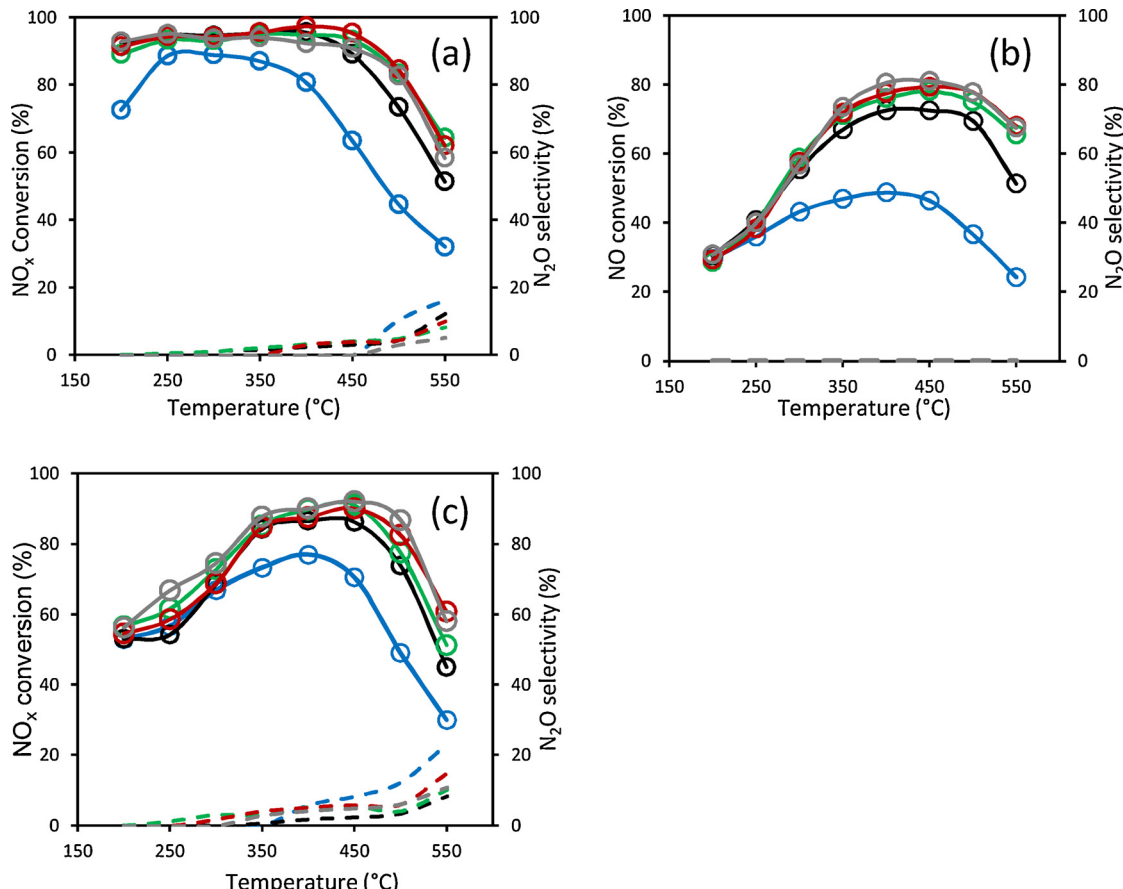


Fig. 6. NO Conversion and N₂O selectivity profiles recorded on CeV_{1-x}W_xO₄ vs. temperature in (a) fast-SCR (NO/NO_x = 0.5), (b) standard-SCR (NO/NO_x = 1) and (c) NO₂-SCR (NO/NO_x = 0.3) conditions : NO conversion in solid line and N₂O selectivity in dashed line – x = 0 (blue); x = 0.02 (black); x = 0.05 (green); x = 0.10 (red); x = 0.15 (grey) (For interpretation of the references to colour in this figure legend, the reader is referred to the web version of this article).

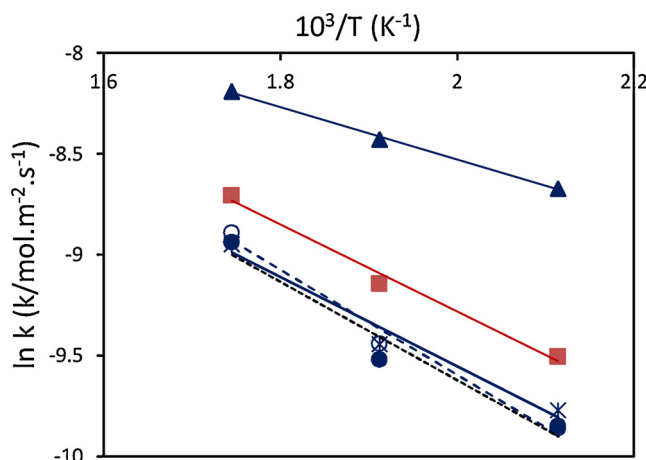


Fig. 7. Arrhenius plots recorded during standard $\text{NH}_3\text{-SCR}$ reaction on aged CeVO_4 (▲), $\text{CeV}_{0.98}\text{W}_{0.02}\text{O}_4$ (■), $\text{CeV}_{0.95}\text{W}_{0.05}\text{O}_4$ (○), $\text{CeV}_{0.90}\text{W}_{0.10}\text{O}_4$ (●) $\text{CeV}_{0.85}\text{W}_{0.15}\text{O}_4$ (*).

nitrogen and ammonia oxidation to NO and N_2O . To this end, this contribution illustrates an attempt to isolate both effects through a careful monitoring of bulk and surface reconstructions at various tungsten concentrations. Indeed, it was earlier found that isolated V^{5+} species in tetrahedral coordination in the zircon-type structure of CeVO_4 lose their redox properties [23]. On the other hand, thermal aging restores these properties due to the occurrence of a slight extraction and agglomeration of vanadia species up to the ultimate formation of surface polymerized VO_x entities with improved redox properties. This led Gillot et al. [23] to the conclusion that redox sites, coupled to a nearest neighbor non reducible site, i.e., $\text{V}-\text{O}-\text{V}$ at the vicinity of $\text{Ce}-\text{O}-\text{V}$ structures, could be responsible of a sharp decrease on the apparent activation energy (10.7 kJ mol^{-1} see Table 3) on CeVO_4 aged at 600°C . As explained, this abnormally low apparent activation energy would reflect the involvement of surface diffusion process which seems consistent with the explanation given by Gao et al. [50] who suggested that ammonia weakly bonded to Lewis acid sites would diffuse more easily to redox sites. This kinetic feature differs from that observed on CeVO_4 aged at 500°C (see Table 3) because the higher values for E_{app} and for the pre-exponential factor would preferentially display the behavior of well-dispersed monomeric VO_x entities being intrinsically much less active than polyvanadates on CeVO_4 aged at 600°C but much more selective assigned to a greater density of Brønsted acid sites. Based on those observations, the differences in the surface structures and related catalytic properties can depend on the aging conditions.

A similar hydrothermal synthesis was implemented for obtaining the mixed $\text{CeV}_{1-x}\text{W}_x\text{O}_4$ oxide composition (with x in the range 0.02–0.15) exhibiting the same tetragonal structure as that observed on the parent material still coexisting with the cubic fluorite structure of CeO_2 but likely in lower extent. The thermal stability has been

preferentially investigated by exposing those sample to 10 vol.% H_2O diluted in air at 600°C which corresponds to the worst aging conditions as aforementioned with an acceleration of surface sintering of mono to polyvanadate species. An important issue resides in the behavior of tungsten accelerating or delaying the diffusion and aggregation of VO_x species. Similarly to previous observations on parent CeVO_4 , the residual CeO_2 cubic phase is still less prone to sinter on tungsten-doped CeVO_4 samples with much lower crystallite sizes compared to that measured on the parent materials (see Table 1). It is also worthwhile to note that tungsten doping strongly delays the thermal sintering of $\text{CeV}_{1-x}\text{W}_x\text{O}_4$ zircon-type phase at increasing tungsten concentration with crystallite size shifting from 85 to 33 nm on $\text{CeW}_{0.85}\text{W}_{0.15}\text{O}_4$. The lack of detection of bulk V_2O_5 species and the absence of loss of vanadium through volatilization still emphasize a strong thermal stability of oxidic vanadium species compared to supported vanadia systems [17]. On the other hand, more complex structural feature changes are observable related the segregation of a cerium-tungsten mixed oxide phase detected from Raman Spectroscopy and XRD analysis compared to the benchmark CeVO_4 . Hence, the concomitant diffusion/aggregation of oxidic vanadium and tungsten species and the relative rates of those processes can drastically modify the bulk and surface composition of $\text{CeV}_{1-x}\text{W}_x\text{O}_4$ materials. The comparison of ^{51}V NMR and EPR measurements also provides useful information. Indeed, the deshielding effect observed on fresh samples ascribed to significant structural distortions due to tungsten substitution strongly attenuates on aged $\text{CeV}_{1-x}\text{W}_x\text{O}_4$ indicating a fast diffusion of oxidic tungsten species. Such a hypothesis seems to be consistent with the formation of bulk Ce-W mixed oxides which could originate the slight discontinuity observed on the bulk reduction process at high temperature for $x > 0.05$. In parallel, the more intense hyperfine structure on aged $\text{CeV}_{1-x}\text{W}_x\text{O}_4$ compared to that described on aged CeVO_4 (see Fig. 4(B)) also reflects a more extensive diffusion and segregation of weakly reducible isolated V^{5+} , originally stabilized in tetrahedral coordination, to more reducible V^{5+} to V^{4+} as VO^{2+} species stabilized in square pyramidal or distorted octahedral environment, especially for highly loaded tungsten samples. In this latter case, similar observations were previously reported by Nova et al. [18] who observed on $\text{V}_2\text{O}_5\text{-WO}_3\text{/TiO}_2$ an agglomeration of monomeric to more reducible polymeric vanadate species at increasing calcination temperature. Accordingly, the same trend could occur during aging at 600°C accelerated by the presence of tungsten.

Now, regarding changes observed at the surface of aged catalysts, it is obvious that tungsten insertion slows down the particle sintering preserving high specific surface area compared to the parent CeVO_4 material. XPS analysis did not reveal sharp changes both on the oxidation state and on the surface composition ascribed to the aging process. As a general trend, XPS analysis shows essentially strong surface tungsten enrichment more accentuated on aged samples by comparing the atomic W/Ce and V/W ratio which is consistent with a faster diffusion of W^{6+} species at the surface compared to V^{5+} . Based on this observation we could hypothesize different types of interactions between vanadium and tungsten according to the extent of aggregation/redisposition processes of VO_x species.

Table 3
Comparison of kinetic parameters on parent CeVO_4 and tungsten doped $\text{CeV}_{1-x}\text{W}_x\text{O}_4$.

Catalyst	Aging Temp. ($^\circ\text{C}$)	$k^{\text{a,b}}$ ($\text{mol s}^{-1} \text{g}^{-1}$)	Normalized k^{b} ($\mu\text{mol s}^{-1} \text{m}^{-2}$)	Pre-exponential factor, A ($\text{mol s}^{-1} \text{m}^{-2}$)	E_{app} (kJ mol^{-1})	TOF ^b (s^{-1})
CeVO_4	500	12.0×10^{-4}	70.6	$(15.2 \pm 1.5) \times 10^{-3}$	21.3 ± 2.1	101
CeVO_4	600	9.9×10^{-4}	171.5	$(2.7 \pm 0.3) \times 10^{-3}$	10.7 ± 1.1	243
$\text{CeV}_{0.98}\text{W}_{0.02}\text{O}_4$	600	10.4×10^{-4}	74.5	$(6.9 \pm 0.7) \times 10^{-3}$	17.9 ± 1.8	n.m.
$\text{CeV}_{0.95}\text{W}_{0.05}\text{O}_4$	600	9.5×10^{-4}	52.5	$(12.6 \pm 1.3) \times 10^{-3}$	21.7 ± 2.2	83
$\text{CeV}_{0.9}\text{W}_{0.1}\text{O}_4$	600	9.8×10^{-4}	52.7	$(8.8 \pm 0.8) \times 10^{-3}$	20.3 ± 2.0	n.m.
$\text{CeV}_{0.85}\text{W}_{0.15}\text{O}_4$	600	10.5×10^{-4}	57.1	$(8.8 \pm 0.8) \times 10^{-3}$	20.3 ± 2.0	n.m.

^a Calculated from Eq. (6).

^b T(reactant) = 200°C .

Table 4

Comparison of the SCR performance of various supported and bulk vanadium-based catalysts.

Catalyst	Feed gas composition	T (reaction) (°C)	X _{NO}	Normalized k ^a (μmol s ⁻¹ m ⁻²)	N ₂ Selectivity	Ref.
V ₂ O ₅ –WO ₃ /TiO ₂ (55 m ² g ⁻¹)	500 ppm NO, 500 ppm NH ₃ , 3 vol.% O ₂ , 10 vol.% H ₂ O, W/F ₀ = 2.7·10 ⁻² g L h ⁻¹	200	0.95	23	85% at 400 °C	[53]
V ₂ O ₅ –WO ₃ /TiO ₂ , Calc. 500 °C (63 m ² g ⁻¹)	750 ppm NO, 840 ppm NH ₃ , 2 vol.% O ₂ , W/ F ₀ = 2.2·10 ⁻² g L h ⁻¹	200	0.10	0.9	82.5% at 500 °C	[18]
Calc. 800 °C (17 m ² g ⁻¹)			0.30	10.9	70% at 500 °C	
CeVO ₄ (32 m ² g ⁻¹)	500 ppm NH ₃ , 500 ppm NO _x , 5 vol.% O ₂ , W/ F ₀ = 3.10 ⁻² g L h ⁻¹	200	0.58	10.3	73.5% at 400 °C	[54]
Aged CeVO ₄ at 600 °C (5.8 m ² g ⁻¹)	400 ppm NH ₃ , 400 ppm NO _x , 8 vol.% O ₂ , 10 vol.% CO ₂ , 10% H ₂ O, W/F ₀ = 4.10 ⁻³ g L h ⁻¹	200	0.30	171.5	100% N ₂ [175–500 °C]	[23]
Aged CeV _{0.95} W _{0.05} VO ₄ at 600 °C (18.3 m ² g ⁻¹)	400 ppm NH ₃ , 400 ppm NO _x , 8 vol.% O ₂ , 10 vol.% CO ₂ , 10% H ₂ O, W/F ₀ = 4.10 ⁻³ g L h ⁻¹	200	0.28	52.5	100% N ₂ [175–550 °C]	This study

^a Calculated according to the mass balance Eq. (6) for an integral reaction assuming a first order kinetic. Normalized rate constants expressed per m² were calculated by taking the specific surface area into account.

^b In the presence of 10 vol.% H₂O and 100 ppm SO₂.

The establishment of relevant correlations between physicochemical properties and catalytic measurements is not evident because tungsten influences differently the catalytic properties of CeV_{1-x}W_xO₄ at low and high temperature. In addition, both redox and acid centers can be kinetically significant depending on the operating conditions. As a general trend, tungsten incorporation broadens the operating window mainly at high temperature above 300 °C compared to the NO_x conversion profile recorded on the parent CeVO₄ catalyst, irrespective of the NO/NO_x ratio. On the contrary, the comparison of kinetic parameters in Table 3, recorded in standard-conditions (NO/NO_x = 1) at low temperature, i.e., 200 °C, shows a slight opposite effect revealing a detrimental effect of tungsten on the normalized rate constant. As a matter of fact, the influence of W on the kinetics of the standard-SCR reaction can be explained based on the evolutions observed on the apparent activation energies and the pre-exponential factors. As seen, an increase of E_{app} from 10.7 to 21.7 kJ mol⁻¹ jointly with an increase of the pre-exponential factor is observable converging to the value obtained on CeVO₄ aged at 500 °C. Ammonia and pyridine adsorption were performed on CeVO₄ and CeV_{0.5}W_{0.5}O₄ as shown in Figs. S2 and S3 (in Supplementary material). As observed, ammonia adsorption do not allow to discriminate Lewis and Brønsted acid sites compared to pyridine adsorption. However, both experiments reveal a sharp increase in the acidic properties on aged CeV_{0.95}W_{0.05}O₄ compared to CeVO₄ (see Table S1) partly ascribed to a greater stabilization of Brønsted acid sites. The tendency originally observed on the calculated normalized rate constants is similar on TOF values based on the pyridine uptake measured at 150 °C (see Table S1). Indeed, a shift to lower value is noticeable on aged CeV_{0.95}W_{0.05}O₄ (83 s⁻¹ instead of 243 s⁻¹ on CeVO₄ aged at 600 °C) converging to the TOF value obtained on CeVO₄ aged at 500 °C. Such observations highlight the suppression of spill-over effect on W-doped sample likely because of dilution effect due to the strong surface tungsten enrichment. The stabilization of more strongly bonded ammonia species on Brønsted instead of Lewis acid sites can also contribute to a lowering of the catalytic performances through the increase in A and E_{app} because of much lower mobility. Hence, no noticeable observation seems to agree with a promoter effect of tungsten at low temperature which suggests that tungsten would essentially play the role of stabilizer in ammonia standard-SCR conditions preserving a high degree of dispersion of monovanadate species.

The stabilization of monovanadate species at high temperature on CeV_{1-x}W_xO₄ is a key point which can partly explain the gain observed on the catalytic performances at high temperature. Structural effect due to tungsten substitution would prevail instead of electronic promoting effects. The tendency of VO_x to form island would be suppressed which suggest well-dispersed VO_x species surrounded by tungstate species according to a random distribution of those species instead of compressing effects exert by tungstate which require increasing surface vanadate concentration. Hence, the selectivity at high temperature

governed by the competition between the selective reduction of NO_x by NH₃ and ammonia oxidation would be more in favor to the first reaction thanks to the stabilization of more selective isolated and/or dimeric VO_x species. The SCR activity is also related to the presence of Brønsted acid sites and it is obvious that tungsten substitution gives rise to a greater density of stronger W-OH Brønsted acid sites than V-OH. A remaining question is related to the chemical environment of W-OH centers ascribed to WO₃ or Ce₄W₉O₃₃ detected from XRD analysis. As previously depicted, there is no Raman line which characterizes the presence of WO₃. Regarding the surface composition given by XPS analysis, a significant increase in the W/Ce ratio is noticeable converging to a value close to 0.4 at increasing tungsten loading which matches correctly with the stoichiometry of Ce₄W₉O₃₃ taking into account the margin of error. Such observations must be compared with previous investigations highlighting a superior SCR-activity and stability of CeWO_x notably at high temperature [55,56].

5. Conclusion

This study reports the impact of the substitution of vanadium by tungsten in tetrahedral coordination in the zircon-type structure of SCR-CeVO₄ catalysts. The CeV_{1-x}W_xO₄ compositions were prepared in soft conditions, with x varying in the range 0.02–0.15, according to a hydrothermal synthesis route leading to the expected tetragonal structure at 180 °C. The solid investigated were preliminary exposed to 10 vol.% H₂O diluted in air at 600 °C. The impact of this aging process was investigated as a function of tungsten loading in order to relate bulk and surface modifications to the catalytic performances in fast-, NO₂- and standard-conditions, corresponding to different NO/NO_x ratio of respectively equal to 0.5, 0.3 and 1.

Bulk and surface changes intensify when vanadium is substituted at increasing tungsten concentrations due to the fact that both W⁶⁺ and V⁵⁺ species can diffuse and segregate inducing significant structural changes and surface segregation evidenced by – (i) the disappearance of structural distortions, – (ii) a strong attenuation of the deshielding effect due to tungsten extraction then inducing a significant surface tungsten enrichment, – (iii) the characterization of an hyperfine structure by EPR on aged CeV_{1-x}W_xO₄ materials ascribed to VO²⁺ centers and related to the formation of more reducible V⁵⁺ species than those originally stabilized in tetrahedral coordination through diffusion and segregation processes. Both observations clearly show that the diffusion of tungsten occurs more readily avoiding an extensive agglomeration at the surface of polymeric VO_x species preserving their selectivity behavior at high temperature in favor of the SCR reaction related to a greater stabilization Brønsted acid sites.

On the other hand, the kinetic behavior differs at low temperature. Indeed, the calculation and the comparison of normalized rate constant, turn-Over-Frequency, apparent activation energy and pre-exponential

factor values led to the conclusion that tungstate in interaction with vanadate species would not originate rate enhancement due electronic promotional effect. On the contrary, a loss of activity is observed which can be explained by structural modifications corresponding to a preferential isolation of well-dispersed monomeric species intrinsically less active than polymeric species. Hence, the presence of tungsten in greater extent would play the role of stabilizer preventing their aggregation to polyvanadate species.

Acknowledgments

This work has achieved within a research project supported by the Agence Nationale de la Recherche (UreeNOx Project, Ref. ANR-11-VPTT-002). We would like to thank Olivier Gardoll, Laurence Burylo, Jean-Charles Morin and Martine Trentesaux for their technical support for Thermal analysis, XRD, infrared spectroscopy and XPS measurements respectively.

Appendix A. Supplementary data

Supplementary material related to this article can be found, in the online version, at doi:<https://doi.org/10.1016/j.apcatb.2018.04.059>.

References

- [1] M.D. Amiridis, R.V. Duevel, I.E. Wachs, *Appl. Catal. A* 20 (1999) 111–122.
- [2] G. Busca, L. Lietti, G. Ramis, F. Berti, *Appl. Catal. B* 18 (1998) 1–36.
- [3] J.P. Chen, R.T. Yang, *Appl. Catal. A* 80 (1992) 135–148.
- [4] L. Lietti, P. Forzatti, *Appl. Catal. B* 3 (1993) 13–35.
- [5] L. Lietti, P. Forzatti, F. Bregani, *Ind. Eng. Chem.* 35 (1996) 3884–3892.
- [6] J.A. Dumesic, N.-Y. Topsøe, H. Topsøe, Y. Chen, T. Slabiak, *J. Catal.* 163 (1996) 409–417.
- [7] N.-Y. Topsøe, *Science* 265 (5176) (1994) 1217–1219.
- [8] I.E. Wachs, *J. Catal.* 124 (1990) 570–573.
- [9] G.T. Went, S.T. Oyama, A.T. Bell, *J. Phys. Chem.* 94 (1990) 4240–4246.
- [10] I.E. Wachs, G. Deo, B.M. Weckhuysen, A. Andreini, M.A. Vuurman, M. de Boer, M. Amiridis, *J. Catal.* 161 (1996) 211–221.
- [11] R. Pérez Vélez, I. Ellmers, H. Huang, U. Bentrup, V. Schünemann, W. Grünert, A. Brückner, *J. Catal.* 316 (2014) 103–111.
- [12] L.J. Alemany, L. Lietti, N. Ferlazzo, P. Forzatti, G. Busca, E. Giamello, F. Bregani, *J. Catal.* 155 (1995) 117–130.
- [13] P.G.W.A. Kompio, A. Brückner, F. Hippler, O. Manoylova, G. Auer, G. Mestl, W. Grünert, *Appl. Catal. B* 217 (2017) 365–367.
- [14] G. Oliveri, G. Ramis, G. Busca, V.S. Escribano, *J. Mater. Chem. C* 3 (1993) 1239–1249.
- [15] Y. He, M.E. Ford, M. Zhu, Q. Liu, U. Tumuluri, Z. Wu, I.E. Wachs, *Appl. Catal. B* 193 (2016) 141–150.
- [16] S. Dahlin, M. Nilsson, D. Bäckström, S.L. Bergman, E. Bengtsson, S.L. Bernasek, L.J. Pettersson, *Appl. Catal. B* 183 (2016) 377–385.
- [17] G. Madia, M. Elsener, M. Koebel, F. Raimondi, A. Wokaun, *Appl. Catal. B* 39 (2002) 180–190.
- [18] I. Nova, L. dall'Aqua, L. Lietti, E. Giamello, P. Forzatti, *Appl. Catal. B* 35 (2001) 31–42.
- [19] Z. Li, J. Li, S. Liu, X. Ren, J. Ma, W. Su, *Catal. Today* 258 (2015) 11–16.
- [20] M.A. Larrubia Vargas, M. Casanova, A. Trovarelli, G. Busca, *Appl. Catal. B* 75 (2007) 303–311.
- [21] F. Liu, H. He, Z. Lian, W. Shan, L. Xie, K. Asakura, W. Yang, H. Deng, *J. Catal.* 307 (2013) 340–351.
- [22] K. Routray, W. Zhou, C.J. Kiely, I.E. Wachs, *ACS Catal.* 1 (2011) 54–66.
- [23] S. Gillot, J.P. Dacquin, C. Dujardin, G. Tricot, P. Granger, *Appl. Catal. B* 218 (2017) 338–348.
- [24] Y. Peng, C. Wang, J. Li, *Appl. Catal. B* 144 (2014) 538–546.
- [25] M.V. Martinez-Huerta, J.M. Coronado, M. Fernandez-Garcia, A. Iglesias-Juez, G. Deo, J.L.G. Fierro, M.A. Bañares, *J. Catal.* 225 (2004) 240–248.
- [26] G. Ramis, G. Busca, V. Lorenzelli, P. Forzatti, *Appl. Catal. B* 64 (1990) 259–278.
- [27] B. Xie, G. Lu, Q. Dai, Y. Wang, Y. Guo, *J. Cluster. Sci.* 22 (2011) 555–561.
- [28] S. Gillot, J.P. Dacquin, C. Dujardin, P. Granger, *Top. Catal.* 59 (2016) 987–995.
- [29] J. Goscianska, M. Ziolk, E. Gibson, M. Daturi, *Catal. Today* 152 (2010) 33–41.
- [30] K.B. Bishoff, *Chem. Eng. Sci.* 22 (1967) 525–530.
- [31] J. Jansson, I. Nova, E. Tronconi (Eds.), *Urea-SCR Technology for DeNO_x After Treatment of Diesel Exhausts*, Springer Science and Business Media, New York, 2014, pp. 65–96.
- [32] L. Chen, *Mater. Lett.* 60 (2006) 1859–1862.
- [33] H.E. Wen, D. Tan, Y. Li, X. Yang, L. Lu, D. Lu, *J. Rare Earths* 33 (2015) 561–566.
- [34] M.A. Banares, I.E. Wachs, *J. Raman Spectrosc.* 33 (2002) 359–380.
- [35] S. Xie, E. Iglesia, A.T. Bell, *J. Phys. Chem. B* 105 (2001) 5144–5152.
- [36] B.M. Reddy, A. Khan, *Langmuir* 19 (2003) 3025–3030.
- [37] A.S. Mamede, E. Payen, P. Grange, G. Poncelet, A. Ion, M. Alifanti, V.I. Parvulescu, *J. Catal.* 223 (2004) 1–12.
- [38] P. Concepcion, H. Knözinger, J.M. Lopez Nieto, A. Martinez-Arias, *J. Phys. Chem. B* 106 (2002) 2574–2582.
- [39] G. Busca, G. Ramis, V. Lorenzelli, *J. Mol. Catal. A* 50 (1989) 231–240.
- [40] A.M. Prakash, L. Kevan, *J. Phys. Chem. B* 104 (2000) 6860–6868.
- [41] M.V. Martinez-Huerta, G. Deo, J.L.G. Fierro, M.A. Bañares, *J. Phys. Chem. C* 111 (2007) 18708–18714.
- [42] Y. Li, Z. Wei, F. Gao, L. Kovarik, R.A.L. Baylon, C.H.F. Peden, Y. Wang, *ACS Catal.* 5 (2015) 3006–3012.
- [43] M. Demeter, M. Neumann, W. Reichelt, *Surf. Sci.* 454–456 (2000) 41–44.
- [44] M. Romeo, K. Bak, J. El Fallah, F. Lenormand, L. Hilaire, *Surf. Int. Anal.* 2 (1993) 508–512.
- [45] M. Kang, E.D. Park, J.M. Kim, J.E. Yie, *Appl. Catal. A* 327 (2007) 261–269.
- [46] X. Lu, C. Song, S. Jia, Z. Tong, X. Tang, Y. Teng, *Chem. Eng. J.* 260 (2015) 776–784.
- [47] I. Nova, C. Ciardelli, E. Tronconi, D. Chatterjee, B. Bandl-Konrad, *Catal. Today* 114 (2006) 3–12.
- [48] M. Koebel, G. Madia, F. Raimondi, A. Wokaun, *J. Catal.* 209 (2002) 159–165.
- [49] M. Inomata, A. Miyamoto, Y. Murakami, *J. Catal.* 62 (1980) 140–148.
- [50] F. Gao, N.M. Washiton, Y. Wang, M. Kollár, J. Szanyi, C.H.F. Peden, *J. Catal.* 331 (2015) 25–38.
- [51] G. Qi, R.T. Yang, *J. Catal.* 217 (2003) 434–441.
- [52] Z. Ma, X. Wu, H. Härelind, B. Wang, *J. Mol. Catal. A* 423 (2016) 172–180.
- [53] L. Chen, J. Li, M. Ge, *J. Phys. Chem. C* 176 (2009) 21177–21184.
- [54] H. Huang, Y. Gu, J. Zhao, W. Wang, *J. Catal.* 326 (2015) 54–68.
- [55] W. Shan, F. Liu, H. He, X. Shi, C. Zhang, *Chem. Commun.* 47 (2011) 8046–8048.
- [56] W. Shan, F. Liu, Y. Yu, H. He, C. Deng, X. Zi, *Catal. Com.* 59 (2015) 226–228.